Supplementary Figures

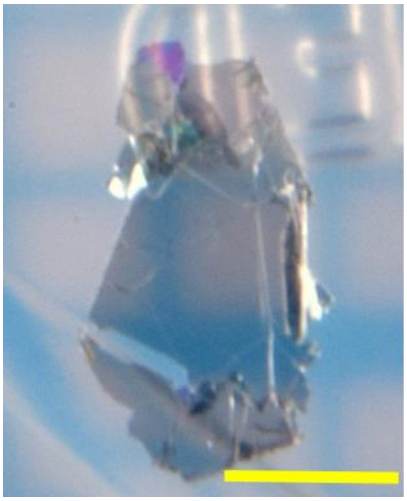

Supplementary Figure 1. Optical image of typical flake-like h-BN sample. Scale bar is 1 mm.

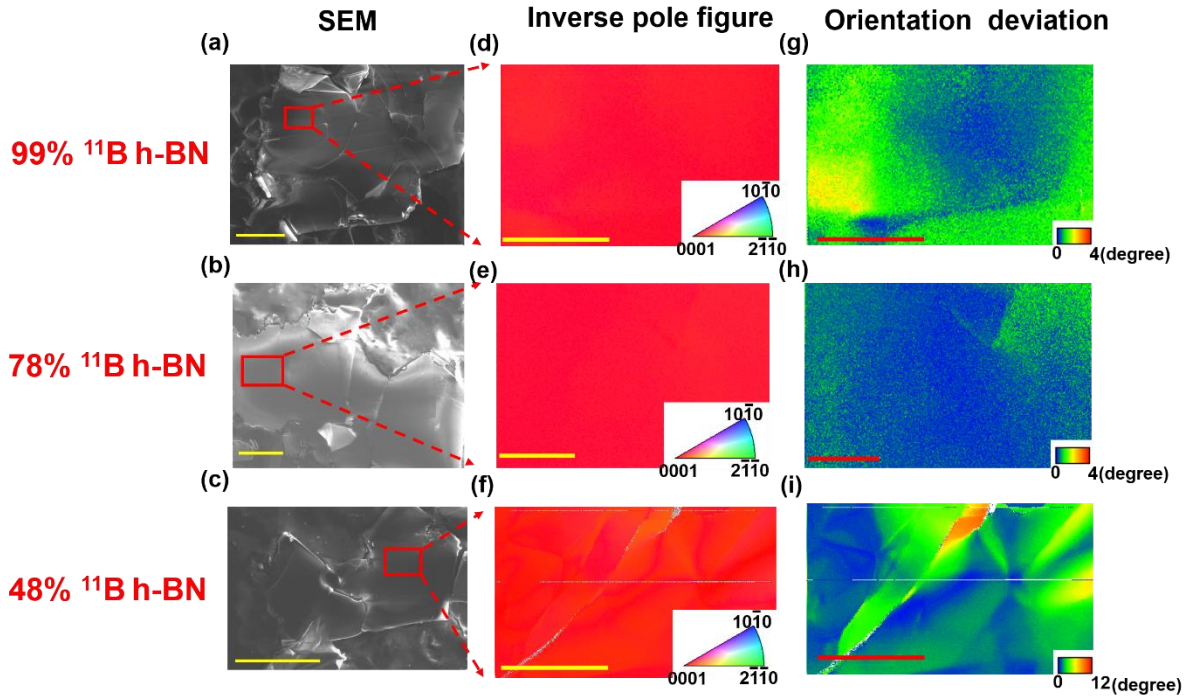

Supplementary Figure 2. Scanning electron microscopy (SEM) images of **(a)** 99% ^{11}B h-BN, **(b)** 78% ^{11}B h-BN and **(c)** 48% ^{11}B h-BN, respectively; scale bars are 200 µm. Electron back-scattered diffraction (EBSD) obtained by scanning a selected area with 1 µm step size: Inverse pole figure for **(d)** 99% ^{11}B h-BN, **(e)** 78% ^{11}B h-BN and **(f)** 48% ^{11}B h-BN; orientation deviation for **(g)** 99% ^{11}B h-BN, **(h)** 78% ^{11}B h-BN and **(i)** 48% ^{11}B h-BN; scale bars are 60 µm. The EBSD maps confirm these crystals have large single crystal domains without evidence of large-scale defects. Small misorientations (tilts) up to about 2° were seen between grains across the 99% ^{11}B h-BN and 78% ^{11}B h-BN samples, while misorientations up to about 6° were present between grains across the 48% ^{11}B h-BN sample.

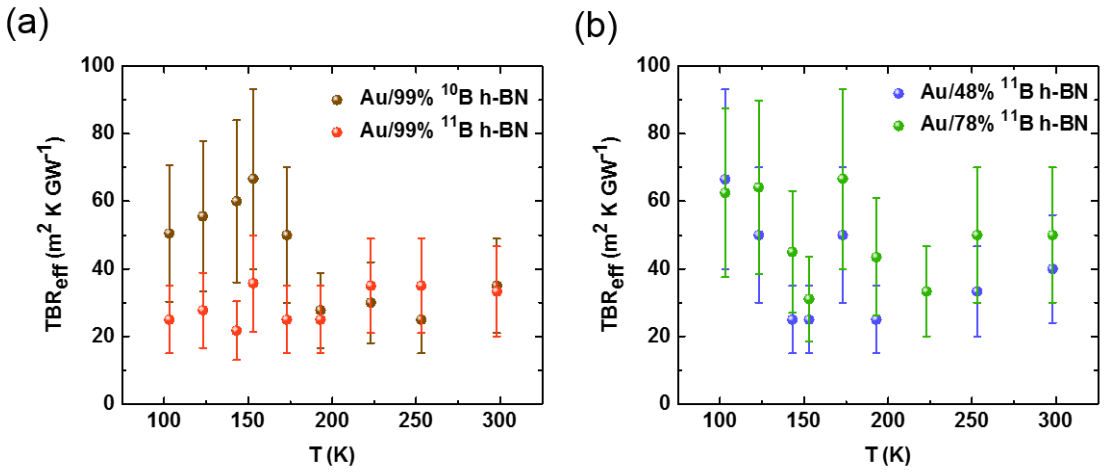

Supplementary Figure 3. Temperature-dependent thermal boundary resistance (TBR_{eff}) between the Au and h-BN interface. **(a)** Au/99% ^{10}B h-BN, Au/99% ^{11}B h-BN; **(b)** Au/78% ^{11}B h-BN, Au/48% ^{11}B h-BN. The error bars in (a-b) correspond to the standard deviation of measured TBR_{eff} results.

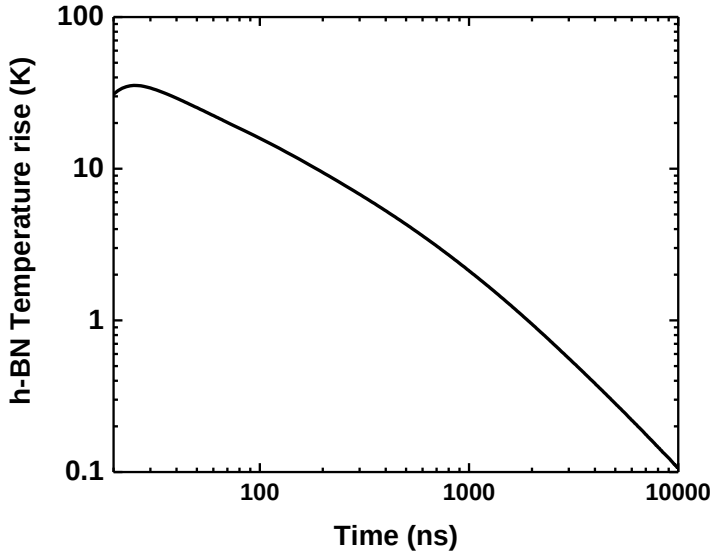

Supplementary Figure 4. Simulated temperature rise (ΔT) at the surface of h-BN. The maximum ΔT is ~45 K. At 100ns, ΔT drops to 10 K and after 1000 ns, ΔT reduces to ~1 K.

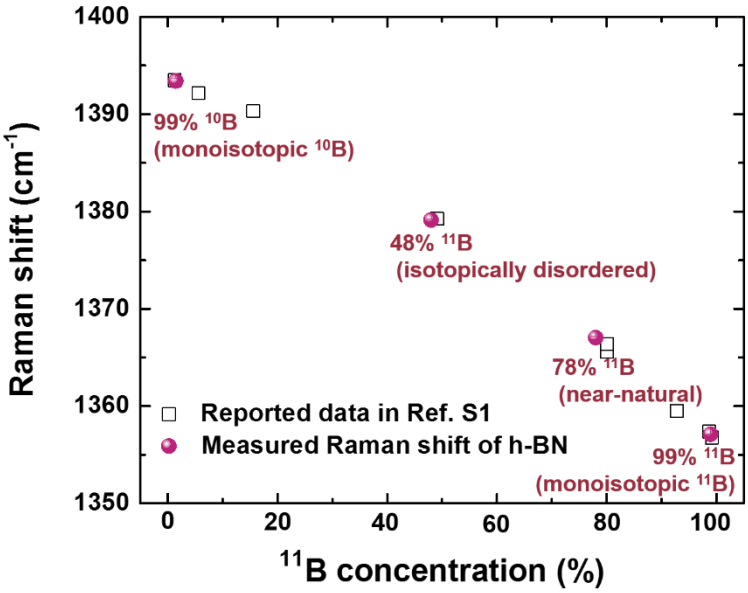

Supplementary Figure 5. Raman shift of the measured BN samples and comparison to data in Ref. S1.

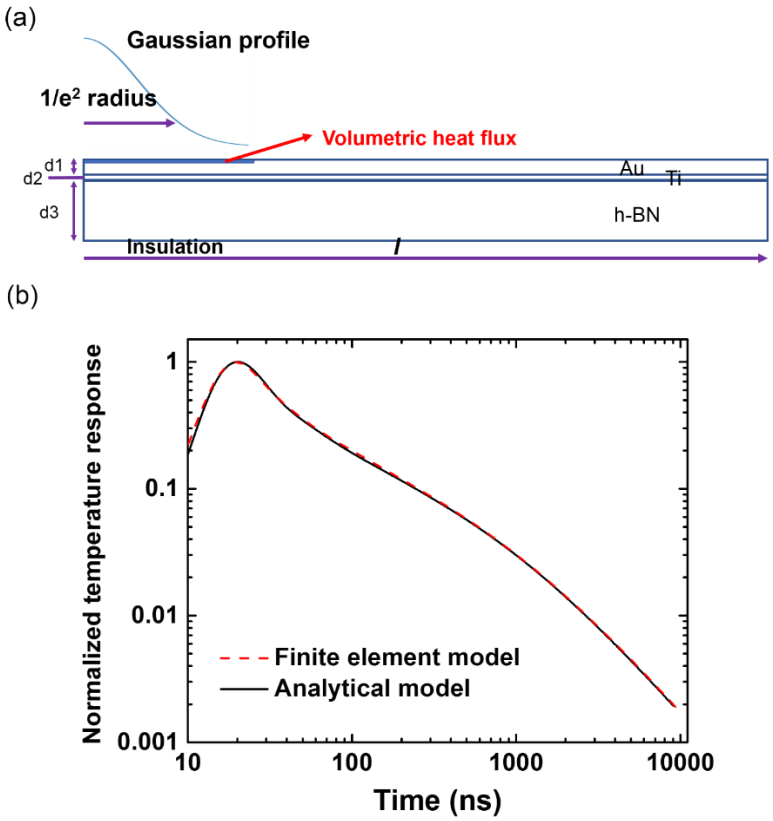

Supplementary Figure 6. **(a)** Thermal transport finite element model considering ½ symmetry of the studied material structure, and geometrical and temporal characteristics of the pump pulse; **(b)** Normalized temperature response solved by the finite element model, overlaid with the solution from the analytical photothermal pulses-induced thermal transport model.

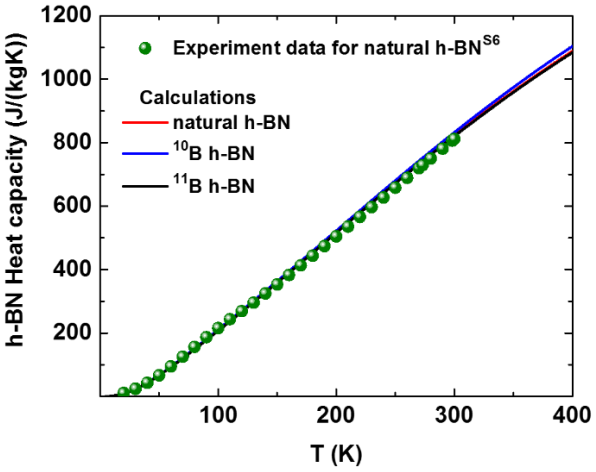

Supplementary Figure 7. Experimentally measured heat capacity for natural h-BN in Ref. S6 and the calculated temperature-dependent heat capacity using Eq. (S1) for natural, monoisotopic ^{10}B and monoisotopic ^{11}B h-BN.

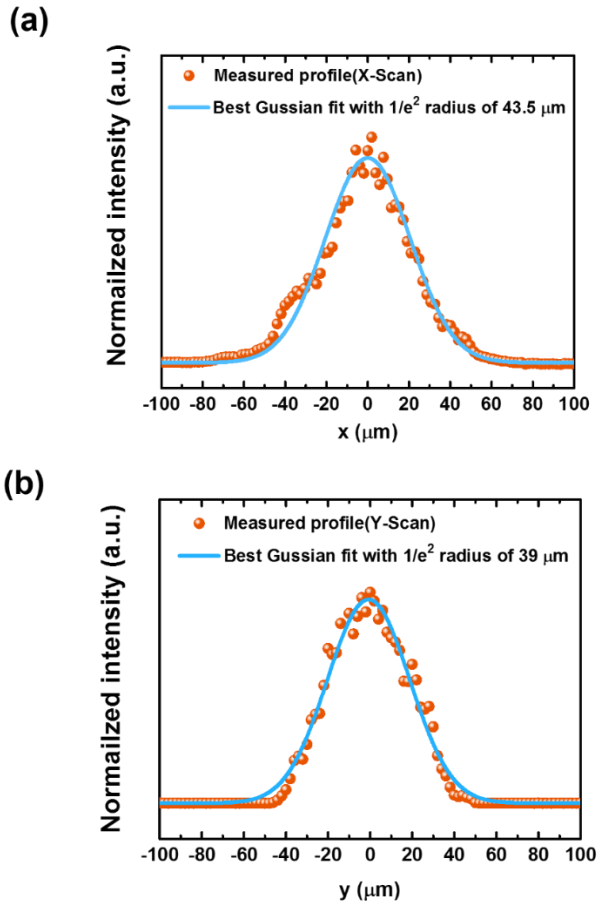

Supplementary Figure 8. Normalized intensity of the pump laser beam as function of position scanned along the **(a)** horizontal-x and **(b)** vertical-y axes, along with their respective Gaussian fits, to determine spot size of the pump laser on the sample surface.

Supplementary Notes

Supplementary note 1: Absolute ratio of the two boron isotopes in the samples studied

In Ref. S1, the absolute ratio of the two boron isotopes was quantified using secondary ion mass spectrometry (SIMS) for several samples of different isotopic enrichments. Through comparison of the SIMS-determined ratios with the in-plane E_{2g} phonon energies extracted from Raman spectroscopy, a relationship was established in Ref. S1, which was used to benchmark the measured Raman shifts here, as shown in Supplementary Figure 5, verifying that the resulting h-BN crystals have the same isotope ratio as the input material used for the material growth.

Supplementary note 2: Validation of the analytical photothermal pulses-induced thermal transport model

The analytical photothermal pulses-induced thermal transport model was validated by finite-element modelling. As shown in Supplementary Figure 6(a), a ½ symmetric two-dimensional finite-element model was built based on the studied material structure, and geometrical and temporal characteristics of the pump pulse. The lateral dimension of the simulation domain (l) was 800 µm, which approximates the h-BN flake sizes shown in Supplementary Figure 1. The thickness of Au, Ti, and h-BN layers (d_1, d_2 and d_3) were 50 nm, 10 nm, and 15 µm, respectively. A volumetric heat flux is employed on a 20 nm x 150 µm area in the Au layer, generated by the absorbed pump laser. Supplementary Figure 6(b) shows the normalized temperature response solved by the finite-element model, overlaid with the solution from the analytical thermal transport model (see main text). The good agreement illustrates the validity of the analytical model for the analysis of the experimental data.

Supplementary note 3: Parameters in the thermoreflectance transient fitting

Thermoreflectance transients are a function of the h-BN out-of-plane (k_z) and in-plane (k_r) thermal conductivities, density, specific heat capacity, thickness of each layer/material, and geometrical and temporal characteristics of the pump pulse. In the transient fitting, except for the anisotropic thermal conductivity (k_z and k_r) of h-BN, and the thermal boundary resistance between the Au transducer and h-BN (TBR_{eff}), all other parameters were treated as fixed values. The Au density was taken as 19300 kg m^{-3} [S2], temperature-dependent specific heat capacity and thermal conductivity were from Ref. S3-S4. The h-BN density values were taken from Ref. S5; note that the isotope effect on density is negligible. The experimentally measured heat capacity in literature is only available for natural h-BN [S6]. We calculated the volumetric temperature-dependent heat capacity (C_V) for natural, monoisotopic ^{10}B and monoisotopic ^{11}B h-BN, plotted in Supplementary Figure 7. C_V was determined from a sum of

heat capacity contributions from each phonon mode labelled by wavevector $\vec{q}$ in branch j in the first Brillouin zone[S7]:

$$C_V = \frac{1}{\rho V_{cell}} \sum_{\vec{q}j} \frac{(\hbar \omega_{\vec{q}j})^2}{k_B T^2} n_{\vec{q}j}(n_{\vec{q}j} + 1) \quad \text{(S1)}$$

where k_B is Boltzmann's constant, V_{cell} is the unit cell volume, $\omega_{\vec{q}j}$ is phonon frequency and $n_{\vec{q}j} = (e^{\hbar\omega_{\vec{q}j}/k_B T} - 1)^{-1}$ is the Bose-Einstein distribution. As shown in Supplementary Figure 7, the calculated C_V for natural h-BN agrees with the experiments, and isotope effects are found to be negligible over the temperature range studied. The calculated C_V is used in the analysis of the TTR measurement.

Au, Ti and h-BN layer thicknesses were input with 50 nm (+/-5%), 10 nm and 15 μm (+/-2 μm). Uncertainties in the h-BN thickness will affect the transients at longer time scales. However, our analytical thermal transport model shows that the transient in the time window 0-3 μs, which we are typically interested in, is independent of h-BN thickness when it is larger than 10 μm. The pump laser spot size was measured by the scanning-slit method. Supplementary Figures 8(a) and 8(b) show scanning-slit profiles along the horizontal (x) and vertical (y) axes, along with their respective Gaussian fits. We measure a $1/e^2$ radius of 41 μm (+/-5%).

Supplementary Reference

S1. Giles, A.J. et al. Ultralow-loss polaritons in isotopically pure boron nitride. *Nat. Mater.* **17**, 134-139 (2018).

S2. Habashi, F. Gold, Physical and Chemical Properties. In: R.H. Kretsinger, V.N. Uversky, and E.A. Permyakov (eds) Encyclopedia of Metalloproteins. Springer, New York, NY (2013).

S3. Feng, B. Li, Z. Zhang, X. Prediction of size effect on thermal conductivity of nanoscale metallic films, *Thin Solid Films* **517,** 2803-2807 (2009).

S4. Takahashi, Y. & Akiyama, H. Heat capacity of gold from 80 to 1000 K, *Thermochim. Acta* **109**, 105-109 (1986).

S5. Vuong, T.Q.P. et al. Isotope engineering of van der Waals interactions in hexagonal boron nitride. *Nat. Mater.* **17**, 152-158 (2018).

S6. Dworkin, A. S., Sasmor, D. J. & Van Artsdalen, E. R. The thermodynamics of Boron Nitride; low-temperature heat capacity and entropy; heats of combustion and formation, *J. Chem. Phys.* **22**, 837-842 (1954).

S7. Ziman, J. M. Electrons and phonons; the theory of transport phenomena in solids, Oxford,: Clarendon Press (1960).